

## MIT Open Access Articles

*Quantifying Mass Transfer Rates in Redox Flow Batteries*

The MIT Faculty has made this article openly available. **Please share** how this access benefits you. Your story matters.

**As Published:** 10.1149/2.0201711JES

**Publisher:** The Electrochemical Society

**Persistent URL:** <https://hdl.handle.net/1721.1/133938>

**Version:** Final published version: final published article, as it appeared in a journal, conference proceedings, or other formally published context

**Terms of use:** Creative Commons Attribution 4.0 International license





## Quantifying Mass Transfer Rates in Redox Flow Batteries

Jarrold D. Milshtein,<sup>a,b,\*</sup> Kevin M. Tenny,<sup>c,\*,\*\*</sup> John L. Barton,<sup>a,d,\*</sup> Javit Drake,<sup>d</sup>  
Robert M. Darling,<sup>a,e,\*\*</sup> and Fikile R. Brushett<sup>a,d,\*\*,z</sup>

<sup>a</sup>Joint Center for Energy Storage Research

<sup>b</sup>Department of Materials Science and Engineering, Massachusetts Institute of Technology, Cambridge, Massachusetts 02139, USA

<sup>c</sup>Department of Chemical and Petroleum Engineering, The University of Kansas, Lawrence, Kansas 66045, USA

<sup>d</sup>Department of Chemical Engineering, Massachusetts Institute of Technology, Cambridge, Massachusetts 02139, USA

<sup>e</sup>United Technologies Research Center, East Hartford, Connecticut 06108, USA

Engineering the electrochemical reactor of a redox flow battery (RFB) is critical to delivering sufficiently high power densities, as to achieve cost-effective, grid-scale energy storage. Cell-level resistive losses reduce RFB power density and originate from ohmic, kinetic, or mass transfer limitations. Mass transfer losses affect all RFBs and are controlled by the active species concentration, state-of-charge, electrode morphology, flow rate, electrolyte properties, and flow field design. The relationship among flow rate, flow field, and cell performance has been qualitatively investigated in prior experimental studies, but mass transfer coefficients are rarely systematically quantified. To this end, we develop a model describing one-dimensional porous electrode polarization, reducing the mathematical form to just two dimensionless parameters. We then engage a single electrolyte flow cell study, with a model iron chloride electrolyte, to experimentally measure cell polarization as a function of flow field and flow rate. The polarization model is then fit to the experimental data, extracting mass transfer coefficients for four flow fields, three active species concentrations, and five flow rates. The relationships among mass transfer coefficient, flow field, and electrolyte velocity inform engineering design choices for minimizing mass transfer resistance and offer mechanistic insight into transport phenomena in fibrous electrodes.

© The Author(s) 2017. Published by ECS. This is an open access article distributed under the terms of the Creative Commons Attribution 4.0 License (CC BY, <http://creativecommons.org/licenses/by/4.0/>), which permits unrestricted reuse of the work in any medium, provided the original work is properly cited. [DOI: 10.1149/2.0201711jes] All rights reserved.



Manuscript submitted March 31, 2017; revised manuscript received May 9, 2017. Published May 31, 2017. *This paper is part of the JES Focus Issue on Mathematical Modeling of Electrochemical Systems at Multiple Scales in Honor of John Newman.*

Grid-scale energy storage has been identified as a key technology for improving sustainability in the electricity generation sector<sup>1</sup> by increasing the efficiency of the existing fossil fuel infrastructure,<sup>2</sup> alleviating intermittency of renewables (e.g., wind, solar),<sup>3</sup> and providing regulatory services.<sup>2</sup> In particular, redox flow batteries (RFBs) have emerged as attractive devices for grid storage.<sup>1</sup> In these rechargeable electrochemical cells, energy is stored and released by reducing or oxidizing electroactive species that are dissolved in liquid-phase electrolyte solutions.<sup>4–7</sup> The electrolytes are housed in large, inexpensive tanks and pumped through a power-converting electrochemical reactor. Within the reactor, a selective membrane, which permits transport of charge-balancing ions but blocks active species, separates two porous electrodes where the respective reduction and oxidation reactions take place. The decoupling of the electrochemical reactor and the energy storage tanks enables independently scalable power (reactor size) and energy capacity (tank size), as well as simplified manufacturing, easy maintenance, and improved safety.<sup>4–7</sup> Designing the electrochemical reactor to deliver sufficiently high power is a critical consideration toward achieving the low battery costs required for economic viability and enabling the efficient delivery of various grid services.<sup>8–10</sup> Cell-level resistive losses in RFBs can originate from one of three areas: ohmic, charge transfer, or mass transport losses. Ohmic losses arise from the current collector, the porous electrodes, or, most significantly, the membrane, while charge transfer losses stem from sluggish reaction kinetics on the electrodes. Current collector and porous electrode ohmic losses can be mitigated through improved cell engineering (i.e., zero-gap architecture).<sup>11,12</sup> Membrane and charge transfer losses tend to be chemistry-specific challenges; for example, all-vanadium RFBs typically utilize specific catalysts or electrode pre-treatments to enhance rates of the desired electrochemical reactions.<sup>13</sup> Mass transport losses are caused by inadequate delivery of active species to the electrode surface and apply to all RFB chemistries.

Mass transport losses limit electrochemical performance due to increases in cell overpotential caused by an inability to deliver reactant to the electrode surface at a sufficient rate.<sup>14</sup> As overpotential losses across the cell increase, the energy efficiency of the battery during cycling will decrease. Further, high overpotentials can limit the accessible state-of-charge (SOC),<sup>15</sup> reducing the practical energy storage capacity of the battery and increasing the effective electrolyte cost.<sup>8,9</sup> In general, improving the convective mass transfer rate can mitigate overpotential loss. Such rates are a function of the active species concentration, SOC, electrolyte velocity, active species diffusion coefficient, flow field design, and electrode structure. Increasing active species concentration is a straightforward approach, and the maximum feasible operating concentration is governed by the least soluble oxidation state of the active species,<sup>16</sup> as well as high viscosity or sluggish kinetics in concentrated electrolytes. At extreme SOC (near 0% or 100%), active species supply for either the forward or backward reactions is limited, decreasing the thermodynamic driving force for reactant delivery. The flow field distributes the liquid electrolyte into the porous electrode, and subsequently the electrolyte must permeate through the electrode pores, where active species can react at the fiber surface. Thus, for a fixed electrolyte chemistry, the flow field and electrode are the most critical components in enhancing convective transport rates, which reduces cell resistance and expands the accessible SOC range.<sup>15</sup> To date, most flow field designs for RFBs have evolved from bipolar plate design for polymer electrolyte fuel cells.<sup>11,17</sup> Commonly, literature reports have investigated the parallel (PFF), serpentine (SFF), interdigitated (IDFF), and flow through (FTFF) flow fields,<sup>14,17,18</sup> though other niche designs exist, such as the spiral<sup>17</sup> or pin-type<sup>19</sup> flow fields. An excellent description of the benefits, shortcomings, and fluid transport mechanisms of the four common RFB flow field types can be found in Ref. 14.

Several recent studies have shown that large performance gains are possible in RFBs through changes in the flow field type, as well as the electrode geometry or morphology.<sup>15,17,18,20–24</sup> While such reports represent excellent engineering efforts to improve RFB power density, increases in mass transfer rates are rarely quantified, arguably due to insufficient knowledge of relevant transport processes within the

\*These authors contributed equally to this work.

\*Electrochemical Society Student Member.

\*\*Electrochemical Society Member.

<sup>z</sup>E-mail: [brushett@mit.edu](mailto:brushett@mit.edu)

specific electrode material.<sup>14</sup> The porous electrodes used for RFBs are typically comprised of loose cylindrical fiber beds where the porosity is  $\sim 70$ – $90\%$ ,<sup>25</sup> but prior electrochemical modeling efforts have described the mass transport rates in RFBs as a function of either mass transfer coefficients for packed bed reactors<sup>18,26</sup> or Bruggeman-corrected diffusion coefficients.<sup>27</sup> Additionally, recent reports have suggested that flow rate dependent reactor performance improvements vary for different flow field types.<sup>17,18,22,28</sup> For example, Darling and Perry observed that increasing flow rate with the IDFF yielded a diminishing rate of return on reactor performance enhancement, hinting at complicated relationships between overall cell performance and flow rate.<sup>17</sup> While several reports have quantified mass transfer rates in electrochemical reactors containing parallel plate electrodes, with and without turbulence promoters,<sup>29,30</sup> only a limited number of studies have investigated mass transfer rates for RFBs with porous electrodes.<sup>23,28</sup>

Quantifying and validating mass transfer rates in a RFB electrode requires a model of sufficient complexity to capture the underlying physics, but of sufficient simplicity to be coupled with experimental studies.<sup>31</sup> Specifically, in the case of extracting mass transfer coefficients, the model must be flexible enough to apply across a broad range of flow cell operating conditions and configurations, but also must not require knowledge of many experimental parameters. Several studies have engaged finite element analysis to offer a detailed description of RFB operation, but these models are computationally intensive and require significant detail.<sup>27,31–33</sup> Specific studies on mass transfer in flow cells with porous electrodes have utilized dimensionless correlations to quantify mass transfer in all-vanadium<sup>28</sup> or zinc-cerium<sup>23</sup> RFBs, but these models can only be applied to direct measurements of the cell's limiting current, which restricts mass transfer coefficient data collection to operating conditions with low flow rates and low active species concentrations. Prior dimensionless porous electrode models by Newman and co-workers are of interest for extracting values from experimental data due to their mathematic reduction to a small number of dimensionless parameters.<sup>34–36</sup> Such models are typically developed for application-specific cases, such as invoking linear or Tafel kinetic descriptions with ohmic losses.<sup>34</sup> As RFBs typically exhibit non-negligible contributions from electrolyte resistivity, charge transfer, and mass transfer, they require development of a new dimensionless porous electrode model of this type.

In this work, we couple a one-dimensional porous electrode model with a single electrolyte flow cell diagnostic technique<sup>18,37–39</sup> to quantify average mass transfer rates for the PFF, SFF, IDFF, and FTFF. First, a one-dimensional, steady-state porous electrode model (Figure 1a), similar to those previously developed by Newman and co-workers,<sup>34–36,40</sup> calculates the overpotential drop across a RFB electrode considering ohmic losses in the electrolyte, Butler-Volmer reaction kinetics, and convective mass transfer limitations. Next, we use single electrolyte flow cell measurements to compare the model prediction to experimental data. This diagnostic method is a proven experimental technique that allows for steady-state measurement of RFB overpotential losses for one electrolyte at 50% SOC (Figure 1b),<sup>18,37–39</sup> without concern for performance degradation caused by crossover or need for reference electrodes.<sup>39</sup> Specifically using a model iron chloride electrolyte, we systematically determine cell polarization for the four flow fields at five flow rates and three active species concentrations. The porous electrode model is then fit to the experimental data, extracting an exchange current density and an average mass transfer coefficient for each flow field and operating condition. The aim of this work is to enable quantitative investigation of the mass transfer enhancements afforded by modifying flow field type and flow rate in RFBs and to provide guiding principles for flow field selection and operating conditions.

### Model Theory

**Thermodynamics and reaction kinetics.**—The single electron transfer, redox reaction of interest is:  $\text{Fe}^{2+} \leftrightarrow \text{Fe}^{3+} + e^-$ . As such,

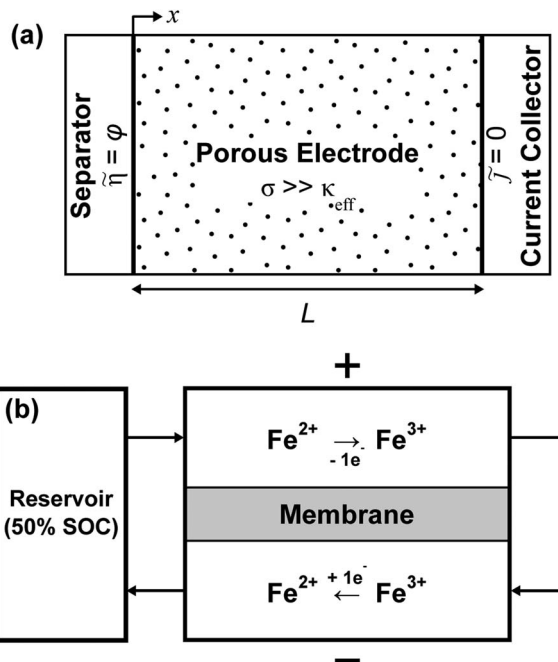


**Figure 1.** (a) Schematic of the one-dimensional porous electrode model, including boundary conditions and key dimensions. (b) Schematic of the single electrolyte flow cell employing the  $\text{Fe}^{2+}/\text{Fe}^{3+}$  couple.

the overall kinetic rate per unit area of electrode ( $\text{mol m}^{-2} \text{s}^{-1}$ ), assuming Butler-Volmer kinetics, can be written as 1, where  $k$  is the heterogeneous reaction rate coefficient ( $\text{m s}^{-1}$ ),  $c^s$  is the active species concentration at the electrode surface ( $\text{mol m}^{-3}$ ),  $n$  is the number of electrons transferred,  $\beta$  is the cathodic transfer coefficient,  $F$  is the Faraday constant ( $\text{C mol}^{-1}$ ),  $R$  is the gas constant ( $\text{J mol}^{-1} \text{K}^{-1}$ ), and  $T$  is temperature (K).<sup>41</sup> The  $a$  and  $c$  subscripts on the reaction rate coefficients denote the anodic and cathodic reactions, respectively.

$$r_k = k_a c_{\text{Fe}^{2+}}^s \exp \left[ \frac{(1-\beta)nF(\Phi_1 - \Phi_2)}{RT} \right] - k_c c_{\text{Fe}^{3+}}^s \exp \left[ \frac{-\beta nF(\Phi_1 - \Phi_2)}{RT} \right] \quad [1]$$

The term  $(\Phi_1 - \Phi_2)$  describes the potential difference (V) across the interface between the solid (electrode fiber) and liquid (electrolyte in pores) phases of the porous electrode. The potential in the solid phase is denoted as  $\Phi_1$ , and the potential in the liquid phase is denoted as  $\Phi_2$ . At equilibrium, the kinetic rate 1 is  $r_k = 0$ . Thus, the equilibrium potential  $(\Phi_1 - \Phi_2)_{eq}$  is:

$$(\Phi_1 - \Phi_2)_{eq} = \frac{RT}{nF} \ln \left( \frac{k_c c_{\text{Fe}^{3+}}^s}{k_a c_{\text{Fe}^{2+}}^s} \right) \quad [2]$$

We can then define the standard potential ( $V^\theta$ , V) under the condition that  $c_{\text{Fe}^{2+}} = c_{\text{Fe}^{2+}}^\theta$  and  $c_{\text{Fe}^{3+}} = c_{\text{Fe}^{3+}}^\theta$ , where  $c_{\text{Fe}^{2+}}^\theta$  and  $c_{\text{Fe}^{3+}}^\theta$  are the standard concentrations (1 M, 298 K) of  $\text{Fe}^{2+}$  and  $\text{Fe}^{3+}$  ions, respectively. For the  $\text{Fe}^{2+} \leftrightarrow \text{Fe}^{3+} + e^-$  reaction,  $V^\theta = 0.771 \text{ V}$  vs. SHE.<sup>42</sup>

$$V^\theta = (\Phi_1 - \Phi_2)^\theta = \frac{RT}{nF} \ln \left( \frac{k_c}{k_a} \right) \quad [3]$$

For the simple iron redox reaction, substituting the standard potential 3 into the reaction rate 1 yields:

$$r_k = k_a c_{\text{Fe}^{2+}}^\theta \exp\left(\frac{(1-\beta)nFV^\theta}{RT}\right) \cdot \left[ \frac{c_{\text{Fe}^{2+}}^s}{c_{\text{Fe}^{2+}}^\theta} \exp\left(\frac{(1-\beta)nF(\Phi_1 - \Phi_2 - V^\theta)}{RT}\right) - \frac{c_{\text{Fe}^{3+}}^s}{c_{\text{Fe}^{3+}}^\theta} \exp\left(\frac{\beta nF(\Phi_1 - \Phi_2 - V^\theta)}{RT}\right) \right] \quad [4]$$

From 4, the exchange current density ( $i_0$ , A m<sup>-2</sup>) can be explicitly defined in 5. Note that in the present formulation,  $i_0$  is invariant with concentration.

$$i_0 = F n k_a c_{\text{Fe}^{2+}}^\theta \exp\left(\frac{(1-\beta)nFV^\theta}{RT}\right) \quad [5]$$

We also define overpotential ( $\eta$ , V) as:

$$\eta = \Phi_1 - \Phi_2 - V^\theta \quad [6]$$

Subsequently, we define the kinetic current density ( $i_k$ , A m<sup>-2</sup>) by substituting 5 and 6 into 4, simultaneously replacing  $\beta$  and  $(1-\beta)$  with a cathodic ( $\alpha_c$ ) and anodic ( $\alpha_a$ ) transfer coefficient, respectively. Additionally, we substitute  $n = 1$  for the iron redox reaction:

$$i_k = i_0 \left[ \frac{c_{\text{Fe}^{2+}}^s}{c_{\text{Fe}^{2+}}^\theta} \exp\left(\frac{\alpha_a F \eta}{RT}\right) - \frac{c_{\text{Fe}^{3+}}^s}{c_{\text{Fe}^{3+}}^\theta} \exp\left(\frac{-\alpha_c F \eta}{RT}\right) \right] \quad [7]$$

**Mass transfer.**—The current density ( $i_n$ , A m<sup>-2</sup>) at the surface of the electrode is directly proportional to the total effective reaction rate ( $r_{\text{eff}}$ , mol m<sup>-2</sup> s<sup>-1</sup>) throughout the electrode 8, assuming the number of electrons transferred is equal to one ( $n = 1$ ):

$$i_n = r_{\text{eff}} F \quad [8]$$

Additionally, the molar fluxes of Fe<sup>2+</sup> and Fe<sup>3+</sup> can be written as shown in 9 and 10, respectively, where  $k_m$  is the mass transfer coefficient (m s<sup>-1</sup>) of iron to or from the electrode surface. Our formulation assumes that  $k_m$  is identical for both Fe<sup>2+</sup> and Fe<sup>3+</sup>.

$$r_{\text{Fe}^{2+}} = k_m (c_{\text{Fe}^{2+}} - c_{\text{Fe}^{2+}}^s) \rightarrow c_{\text{Fe}^{2+}}^s = c_{\text{Fe}^{2+}} - r_{\text{eff}} F k_m^{-1} = c_{\text{Fe}^{2+}} - i_n F^{-1} k_m^{-1} \quad [9]$$

$$r_{\text{Fe}^{3+}} = k_m (c_{\text{Fe}^{3+}}^s - c_{\text{Fe}^{3+}}) \rightarrow c_{\text{Fe}^{3+}}^s = c_{\text{Fe}^{3+}} + r_{\text{eff}} F k_m^{-1} = c_{\text{Fe}^{3+}} + i_n F^{-1} k_m^{-1} \quad [10]$$

The total concentration of iron ( $c_{\text{Fe}^{2+}} + c_{\text{Fe}^{3+}}$ ) is constant in the diffusion layer near the surface of the electrode according to 9 and 10; we neglect migration in the diffusion layer due the presence of excess supporting electrolyte. Next, a combined expression for current density at the electrode surface includes reaction kinetics and mass transfer. We substitute 9 and 10 into 7 to relate current density to a mass transfer coefficient:

$$i_n = i_0 \left[ \frac{(c_{\text{Fe}^{2+}} - i_n F^{-1} k_m^{-1})}{c_{\text{Fe}^{2+}}^\theta} \exp\left(\frac{\alpha_a F \eta}{RT}\right) - \frac{(c_{\text{Fe}^{3+}} + i_n F^{-1} k_m^{-1})}{c_{\text{Fe}^{3+}}^\theta} \exp\left(\frac{-\alpha_c F \eta}{RT}\right) \right] \quad [11]$$

We then rearrange 11, solving explicitly for  $i_n$ , with the assumption that the standard state concentrations for Fe<sup>2+</sup> and Fe<sup>3+</sup> are identical ( $c^\theta = c_{\text{Fe}^{2+}}^\theta = c_{\text{Fe}^{3+}}^\theta$ ):

$$i_n = \frac{i_0 \left[ \frac{c_{\text{Fe}^{2+}}^s}{c^\theta} \exp\left(\frac{\alpha_a F \eta}{RT}\right) - \frac{c_{\text{Fe}^{3+}}^s}{c^\theta} \exp\left(\frac{-\alpha_c F \eta}{RT}\right) \right]}{1 + \frac{i_0}{F k_m c^\theta} \exp\left(\frac{\alpha_a F \eta}{RT}\right) + \frac{i_0}{F k_m c^\theta} \exp\left(\frac{-\alpha_c F \eta}{RT}\right)} \quad [12]$$

For the single electrolyte flow cell employed in this work, the electrolyte remains at 50% SOC with constant iron concentration, implying that  $c = c_{\text{Fe}^{2+}} = c_{\text{Fe}^{3+}}$  for all experiments. We can also define the limiting current density,  $i_l = F k_m c$  (A m<sup>-2</sup>), and substitute into 12:

$$i_n = \frac{i_0 \frac{c}{c^\theta} \left[ \exp\left(\frac{F \eta}{2RT}\right) - \exp\left(\frac{-F \eta}{2RT}\right) \right]}{1 + \frac{i_0}{i_l} \frac{c}{c^\theta} \left[ \exp\left(\frac{F \eta}{2RT}\right) + \exp\left(\frac{-F \eta}{2RT}\right) \right]} \quad [13]$$

Additionally, we assume  $\alpha_a = \alpha_c = 0.5$  for the Fe<sup>2+</sup> ↔ Fe<sup>3+</sup> + e<sup>-</sup> reaction, in agreement with experimental reports.<sup>43</sup> As such, we can simplify 13 to 14:

$$i_n = \frac{i_0 \frac{c}{c^\theta} \left[ \exp\left(\frac{F \eta}{2RT}\right) - \exp\left(\frac{-F \eta}{2RT}\right) \right]}{1 + \frac{i_0}{i_l} \frac{c}{c^\theta} \left[ \exp\left(\frac{F \eta}{2RT}\right) + \exp\left(\frac{-F \eta}{2RT}\right) \right]} \quad [14]$$

Finally, the current density for one electrode within the single electrolyte flow cell can be written in terms of hyperbolic functions. Note that in the following experimental work, with the single electrolyte cell, the open circuit potential is equivalent to  $V^\theta$  in all experiments because the electrolyte is fixed at 50% SOC with low conversion per pass, indicating that  $\eta$  has no concentration dependence.

$$i_n = \frac{2i_0 \frac{c}{c^\theta} \sinh\left(\frac{F \eta}{2RT}\right)}{1 + 2 \frac{i_0}{i_l} \frac{c}{c^\theta} \cosh\left(\frac{F \eta}{2RT}\right)} \quad [15]$$

**One-Dimensional porous electrode.**—Now that the current density has been related to the applied overpotential, we next assume that the conductivity of the electrode fibers is much greater than the effective electrolyte conductivity ( $\sigma \gg \kappa_{\text{eff}}$ ). For physical justification, the conductivity of dry carbon paper electrodes is typically  $\sigma \approx 3000$  mS cm<sup>-1</sup>,<sup>18</sup> whereas the electrolyte conductivities measured in this work are  $\kappa_{\text{eff}} \leq 305$  mS cm<sup>-1</sup> (Figure 5). As such, the potential gradient in the electrode fibers is negligible in comparison to the potential gradient in the electrolyte:

$$\nabla \Phi_1 = 0 \quad [16]$$

To good approximation, Ohm's law holds in the electrolyte due to the presence of excess supporting electrolyte, allowing us to relate the ionic current density through the electrolyte ( $i_2$ , A m<sup>-2</sup>) to the potential gradient in the electrolyte phase of the porous electrode 17, where  $x$  is the position in the porous electrode ( $0 < x < L$ ). Note that  $i_2|_{x=0}$  represents the ionic current density passing through the separator and is equal to the total current density through the cell.

$$i_2 = -\kappa_{\text{eff}} \frac{d\Phi_2}{dx} = \kappa_{\text{eff}} \frac{d\eta}{dx} \quad [17]$$

To maintain charge balance, the divergence of the ionic current density along the electrode thickness balances the faradaic current passing through the electrode ( $a \cdot i_n$ ), within a plane located at  $x$ , where  $a$  is the electrode surface area per unit volume (m<sup>2</sup> m<sup>-3</sup>):

$$\frac{di_2}{dx} = a i_n \quad [18]$$

Finally, we can combine 15, 17, and 18 to relate overpotential to current:

$$\frac{d^2 \eta}{dx^2} = \frac{a}{\kappa_{\text{eff}}} i_n(\eta) = \frac{a i_0}{\kappa_{\text{eff}}} f(\eta) \quad [19]$$

Where the function,  $f(\eta) = i_n/i_0$ , is shown in 20. In the following experimental work,  $c$  is fixed by the electrolyte concentration and SOC and does not vary as a function of position in the electrode due to low conversion per pass. As such,  $c$  is a fixed parameter for each experimental set-up.

$$f(\eta) = \frac{2 \frac{c}{c^\theta} \sinh\left(\frac{F \eta}{2RT}\right)}{1 + 2 \frac{i_0}{i_l} \frac{c}{c^\theta} \cosh\left(\frac{F \eta}{2RT}\right)} \quad [20]$$



**Dimensionless form and boundary conditions.**—The dimensionless overpotential ( $\tilde{\eta}$ ) is defined as the overpotential normalized by the thermal potential ( $RT/F$ , V):

$$\tilde{\eta} = \frac{F\eta}{RT} \quad [21]$$

The dimensionless position inside the electrode is defined as the position normalized by the electrode thickness ( $L$ , m):

$$\tilde{x} = \frac{x}{L} \quad [22]$$

$\theta$  is defined as the ratio of the exchange and limiting current densities:

$$\theta = \frac{i_0}{i_l} \quad [23]$$

Finally, the dimensionless bulk active species concentration ( $\tilde{c}$ ) is defined as the bulk concentration normalized by the standard state concentration:

$$\tilde{c} = \frac{c}{c^\theta} \quad [24]$$

We can write 19 in dimensionless form by normalizing the total cell current density by the thermal potential, electrode thickness, and effective electrolyte conductivity, while defining a dimensionless exchange current density ( $v^2$ ):

$$\frac{d^2\tilde{\eta}}{d\tilde{x}^2} = \frac{Fai_0L^2}{\kappa_{\text{eff}}RT} f(\tilde{\eta}) = v^2 f(\tilde{\eta}) \quad [25]$$

As such, we must also define the dimensionless reaction rate,  $f(\tilde{\eta})$ , as a function of the dimensionless overpotential,  $f(\tilde{\eta})$ , with  $\theta$  and  $\tilde{c}$  as parameters:

$$f(\tilde{\eta}) = \frac{2\tilde{c} \sinh\left(\frac{\tilde{\eta}}{2}\right)}{1 + 2\theta\tilde{c} \cosh\left(\frac{\tilde{\eta}}{2}\right)} \quad [26]$$

The dimensionless ionic current density can then be derived from  $\tilde{\eta}(\tilde{x})$  as:

$$\tilde{j}(\tilde{x}) = -\frac{1}{2} \frac{d\tilde{\eta}}{d\tilde{x}} \quad [27]$$

At the separator-electrode interface (Figure 1a, left), we impose a constant overpotential boundary condition ( $\varphi$ ) such that:

$$\varphi = \tilde{\eta}|_{\tilde{x}=0} \quad [28]$$

Ionic current cannot flow at the electrode-current collector interface (Figure 1a, right), providing the basis for a zero ionic current density boundary condition:

$$\tilde{j}|_{\tilde{x}=1} = -\frac{1}{2} \frac{d\tilde{\eta}}{d\tilde{x}} \Big|_{\tilde{x}=1} = 0 \quad [29]$$

In the present analysis, we numerically solve for the dimensionless overpotential as a function of dimensionless position in the electrode,  $\tilde{\eta}(\tilde{x})$ , and derive the dimensionless ionic current density,  $\tilde{j}(\tilde{x})$ . The Supplementary Material defines integrals that could be used as an alternative method to compute  $\tilde{\eta}(\tilde{x})$  and  $\tilde{j}(\tilde{x})$ .

## Experimental

**Electrolyte, electrode, and membrane preparation.**—Iron (II) chloride tetrahydrate ( $\text{FeCl}_2 \cdot 4\text{H}_2\text{O}$ , > 99%), iron (III) chloride hexahydrate ( $\text{FeCl}_3 \cdot 6\text{H}_2\text{O}$ , 97%), and hydrochloric acid (HCl, 37 wt% balance water) were all purchased from Sigma Aldrich and used as received. Appropriate amounts of the iron (II/III) chloride hydrates were combined with HCl and deionized water (18 m $\Omega$ , Millipore) to produce stock electrolytes containing 0.2, 0.5, or 0.8 M iron chloride at 50% SOC ( $\text{Fe}^{2+/3+}$ ) in 2 M HCl. Carbon paper electrodes (25AA, SGL Group) were thermally treated at 500 °C for 30 h to improve hydrophilicity.<sup>13</sup> Nafion 115 (N115, DuPont) was soaked overnight in 2 M HCl, at room temperature, before serving as the membrane in all flow cell experiments.

**Electrolyte conductivity measurements.**—Electrolyte conductivity measurements were collected using a two electrode, Swagelok style conductivity cell. The conductivity cell was identical to prior literature descriptions,<sup>38,44</sup> except now employing graphite current collectors, instead of stainless steel, to mitigate corrosion in the presence of HCl. Conductivity standards containing 0.5, 1.5, 2.0, 3.5, and 6.0 M HCl were prepared, and a 7-point calibration curve was constructed by measuring cell impedance at 0 °C or 25 °C, according to prior literature procedures.<sup>38,44</sup> Known conductivity values of the standard solutions were collected from reference tables.<sup>42</sup>

**Flow battery preparation and experiment.**—The zero-gap<sup>11</sup> flow cell design, with a geometric active area of 2.55 cm<sup>2</sup>, is reported in prior literature.<sup>16,38,44</sup> The interdigitated (IDFF), parallel (PFF), flow through (FTFF), and serpentine flow fields (SFF) were manufactured in-house using 3.18 mm thick impermeable graphite (G347B, MWI, Inc.). The exact dimensions of the flow fields are provided within two dimensional engineering drawings in the Supplementary Material (Figures S1–S4). Two layers of heat treated carbon paper electrode were used on each side of the cell and sealed with Teflon gaskets. The gaskets compressed the electrodes by  $20 \pm 2\%$ . A glass scintillation vial, sealed with a rubber stopper, served as the reservoir for 10 mL of electrolyte. The electrolyte was continuously sparged with nitrogen gas (Airgas,  $\geq 99.999\%$ ). The electrolyte was pumped from the reservoir to the cell assembly using a peristaltic pump (Masterflex L/S Series) through perfluoroalkoxy alkane tubing (3.2 mm inner diameter, Swagelok), connected to the cell and pump head, with Norprene tubing (3.2 mm inner diameter, Masterflex) inside the pump head. All flow cell components and pump tubing were selected due to their chemical compatibility with the electrolytes of interest.

Prior to beginning polarization measurements, all flow cells were preconditioned by applying a constant cell potential of 100 mV for 30 min using an Arbin battery tester (BTS-200). The electrolyte flow rate was 3 mL min<sup>−1</sup> during the cell preconditioning step. After preconditioning, a high-frequency impedance measurement (Biologic VMP3) was collected over the frequency range of 20 kHz to 1 Hz at open circuit potential to determine the ohmic contribution ( $R_\Omega$ ) to the total cell resistance. Polarization data was collected by applying potentiostatic holds for 2 min in 25 mV increments from 0 V to 0.2 V, with data recording every 1 s. Polarization curves were generated by identifying the mean of the last 50% of data points from the current response. The overpotential loss associated with the ohmic contribution to the total cell resistance (contributions from the membrane, contact resistances, current collectors, and test leads) was subtracted from the overpotential measurement at each current to generate  $iR$ -corrected polarization data in accordance with literature precedence.<sup>17</sup> The solid conductivity of the electrodes contributes negligibly to the high-frequency impedance. Polarization measurements were collected at five flow rates (0.5, 1, 2, 3, and 10 mL min<sup>−1</sup>) and three active species concentrations (0.2, 0.5, and 0.8 M  $\text{Fe}^{2+/3+}$ ) for each flow field design.

## Model Trends

The porous electrode model in 25 and 26 describes the dimensionless overpotential distribution as a function of position in the porous electrode. Figure 2 shows representative overpotential distributions for multiple values of  $v^2$  and  $\theta$ , at fixed concentration ( $\tilde{c} = 1$ ). For all plots in Figure 2, the dimensionless overpotential at the separator-electrode interface is fixed at  $\tilde{\eta}|_{\tilde{x}=0} = \varphi = 3$  (Figure 1a, left), which corresponds to an electrode overpotential of  $\eta = 77$  mV under the experimental conditions employed later in this work. At the electrode-current collector interface ( $\tilde{x} = 1$ ), the overpotential achieves a plateau, as dictated by the zero ionic current boundary condition at the electrode-current collector interface (Figure 1a, right). Generally, as  $v^2$  increases, the overpotential gradient in the electrode becomes larger. A higher value of  $v^2$  indicates faster charge transfer kinetics and subsequently larger exchange current density. Similarly, as  $\theta$  decreases, the overpotential

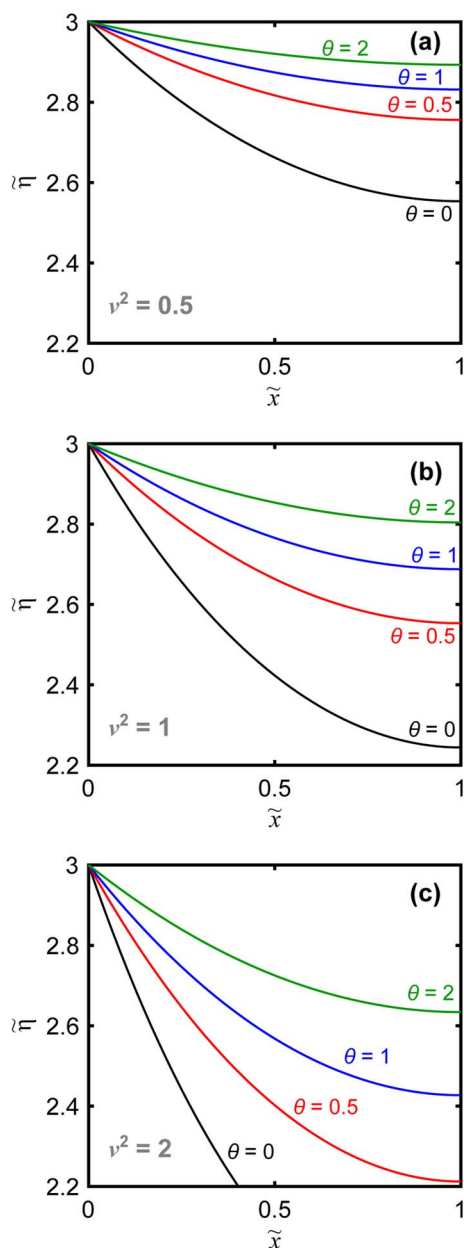


**Figure 2.** Dimensionless representation of overpotential ( $\tilde{\eta}$ ) as a function of position in the porous electrode ( $\tilde{x}$ ) for multiple values of  $v^2$  and  $\theta$ . (a)  $v^2 = 0.5$ , (b)  $v^2 = 1$ , and (c)  $v^2 = 2$ . For all analyses, the dimensionless concentration is set equal to unity ( $\tilde{c} = 1$ ).

gradient also becomes larger. Smaller values of  $\theta$  imply larger limiting currents and higher mass transfer rates, and  $\theta = 0$  represents the case of infinitely fast mass transfer. Interestingly, increasing the exchange (larger  $v^2$ ) or limiting (smaller  $\theta$ ) currents achieves same effect of a steeper overpotential gradient in the electrode.

To better understand the roles of the exchange and limiting current densities in defining electrode performance, consider the dimensionless ionic current density distribution profiles in Figure 3, which are derived from the overpotential profiles in Figure 2, for multiple values of  $v^2$  and  $\theta$ . Note that for all current density distributions in Figure 3,  $\tilde{j}|_{\tilde{x}=1} = 0$ , in accordance with the zero ionic current boundary condition at the electrode-current collector interface (Figure 1a, right). Given that the ionic current density is directly proportional to the gradient in electrode overpotential (Eq. 27), a larger overpotential gradient yields greater current densities across the electrode, implying improved electrode performance. Thus, increasing  $v^2$  or decreasing  $\theta$

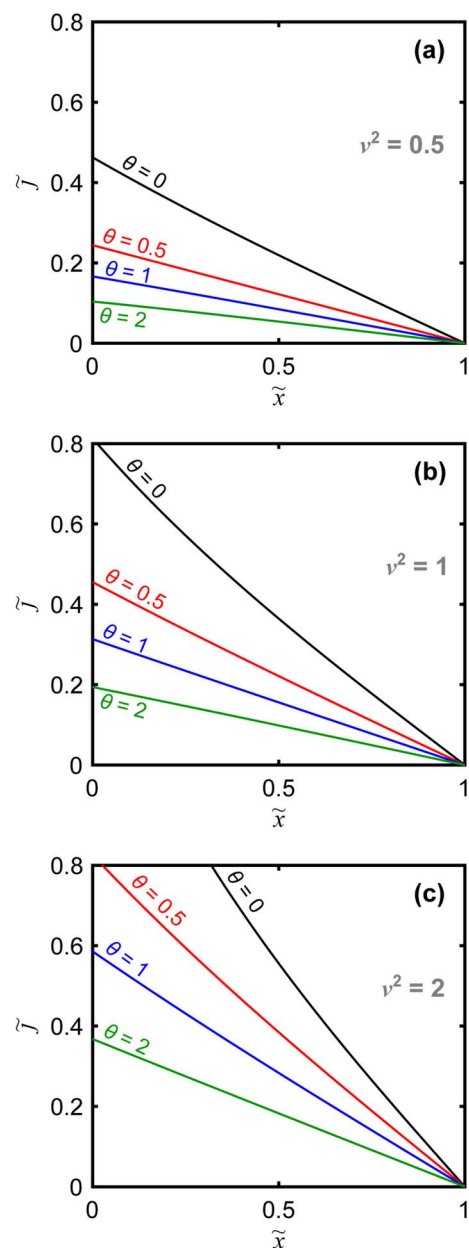


**Figure 3.** Dimensionless representation of ionic current ( $\tilde{j}$ ) as a function of position in the porous electrode ( $\tilde{x}$ ) for multiple values of  $v^2$  and  $\theta$ . (a)  $v^2 = 0.5$ , (b)  $v^2 = 1$ , and (c)  $v^2 = 2$ . For all analyses, the dimensionless concentration is set equal to unity ( $\tilde{c} = 1$ ).

leads to a better performing electrode because a larger current density can be achieved for the same applied potential drop across the porous electrode. Physically, this trend originates because a higher exchange current density or larger limiting current density will increase the total current density through the electrode by alleviating charge transfer or mass transfer limitations, respectively.

The earlier assumption that the electronic conductivity of the electrode fibers is much larger than the electrolyte conductivity ( $\sigma \gg \kappa_{\text{eff}}$ ) implies that the path of least resistance for charge to exit the porous electrode is through the electrode fibers. As such, the electrode prefers to push current out of the electrolyte and into the electrode fibers, which can only be achieved by invoking the electrochemical reaction to transfer charge from the active material to the electrode fibers. The electrochemical reaction, however, is limited by the reaction rate ( $v^2$ ) and mass transfer ( $\theta$ ). Consequently, higher reaction (larger  $v^2$ ) or

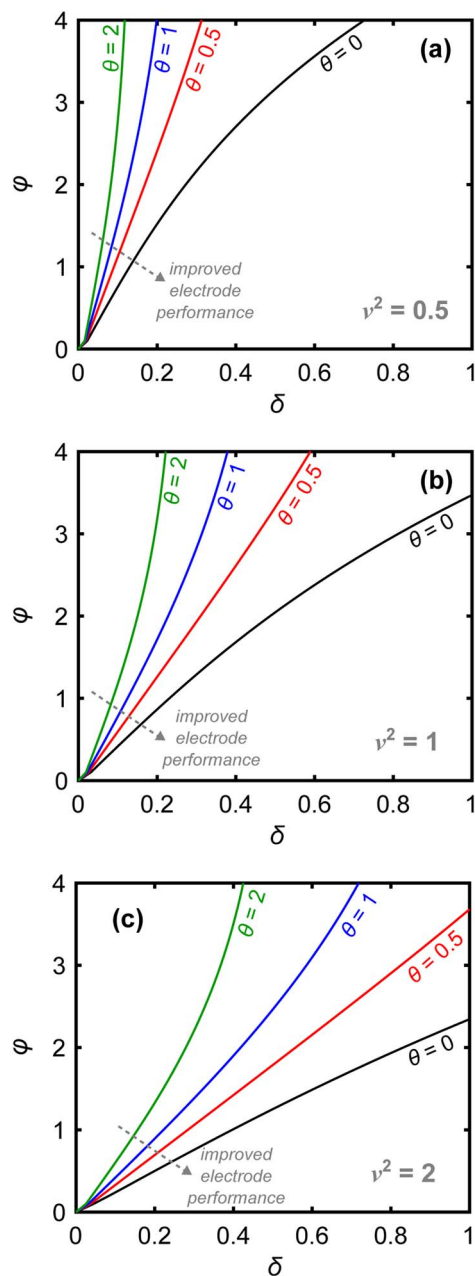


**Figure 4.** Dimensionless representation of computed polarization, plotting overpotential at the separator-electrode interface ( $\phi$ ) as a function of current density ( $\delta$ ) for multiple values of  $v^2$  and  $\theta$ . (a)  $v^2 = 0.5$ , (b)  $v^2 = 1$ , and (c)  $v^2 = 2$ . For all analyses, the dimensionless concentration is set equal to unity ( $\bar{c} = 1$ ).

mass transfer (smaller  $\theta$ ) rates, yield a larger gradient in the ionic current and subsequently larger gradient in the electrode overpotential. Essentially, slow mass transfer or reaction rates have the same physical effect in the porous electrode because the electrode cannot quickly transfer the flow of charge from the electrolyte to the electrode.

From the computed overpotential and current density distributions in the porous electrode, we can develop dimensionless polarization curves that describe the current-overpotential characteristic of the electrode. Figure 4 shows dimensionless polarization curves, plotting the dimensionless overpotential at the separator-electrode interface ( $\phi$ ) as a function of the dimensionless current density passing through

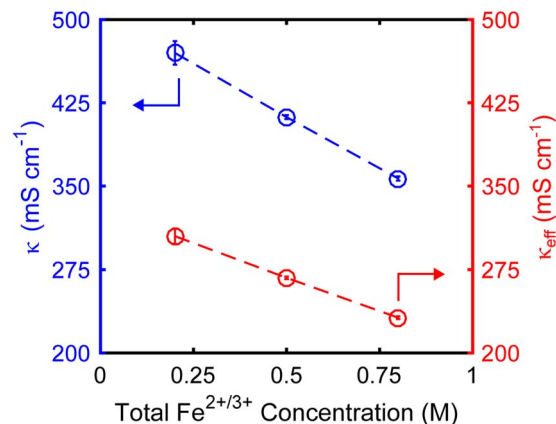


**Figure 5.** Electrolyte conductivity (left, blue) as a function of active species concentration at 50% SOC, with 2 M HCl supporting electrolyte. The effective electrolyte conductivity (right, red) is calculated from the Bruggeman relation, assuming  $\epsilon = 0.75$  and  $b = 1.5$ .

the separator ( $\delta$ ), which is defined in 30.

$$\delta = \frac{FL}{2\kappa_{\text{eff}}RT} \cdot |i_2|_{x=0} \quad [30]$$

Now the electrode performance dependence on  $v^2$  and  $\theta$  becomes even more apparent. As  $v^2$  increases or  $\theta$  decreases, the electrode overpotential at a fixed current decreases, implying that the electrode can drive a larger current for a smaller overpotential loss. Additionally, the role of mass transfer at large overpotentials becomes apparent; slower mass transfer rates (larger  $\theta$ ) drive the polarization curve toward limiting current more quickly. Ultimately, this model captures the effects of charge transfer and mass transfer as they impact the overall electrode polarization.

### Experimental Results and Model Fitting

Conveniently, the dimensionless porous electrode model contains only two parameters ( $v^2$  and  $\theta$ ), enabling relatively simple curve fitting of the model to experimental data. Extracting dimensional information from these curve fits, however, requires knowledge of the electrolyte conductivity because the dimensionless exchange current is normalized by the effective electrolyte conductivity (Eq. 25). Figure 5 shows measured and effective conductivities of the electrolytes employed in this work. All electrolytes contain a 50% SOC mix of  $\text{Fe}^{2+/3+}$  with 2 M HCl, and the total iron concentration is denoted on the x-axis in Figure 5. Notably, the electrolyte conductivity decreases with increasing iron concentration, most likely caused by increasing electrolyte viscosity and inter-species interactions. The electrolyte conductivities ( $\kappa$ ) are intrinsic to the electrolyte, and these conductivities are corrected using the Bruggeman relation 31 to compute an effective electrolyte conductivity ( $\kappa_{\text{eff}}$ ) within the porous electrode.<sup>35</sup> For this work, we assume a compressed electrode porosity,  $\epsilon = 0.75$ , as measured in a recent experimental study of SGL 25AA carbon paper morphology under compression<sup>25</sup> and a Bruggeman coefficient,  $b = 1.5$ .<sup>35</sup>

$$\kappa_{\text{eff}} = \kappa \epsilon^b \quad [31]$$

The single electrolyte flow cell configuration (Figure 1b) is a useful diagnostic tool for investigating flow cell performance.<sup>18,37–39</sup> In this configuration, a flow cell is connected to a single reservoir with one active species present at 50% SOC. The electrolyte stream circulates through the flow cell; the active material is oxidized at the positive electrode and then reduced at the negative electrode before returning to the reservoir. As such, the reservoir SOC does not change with time, and the cell operates at steady state over a wide range of flow rates and current densities.<sup>39</sup> Additionally, crossover effects will not degrade the cell performance since the same electrolyte composition

is present on both sides of the cell.<sup>18</sup> This diagnostic technique permits cell-level analysis without reference electrodes, since nearly identical electrochemical processes are taking place on either side of the cell.<sup>18</sup> When this technique is employed with low active species conversion per pass (i.e., small change in SOC), overpotential losses due to the electrodes can simply be divided across the two sides.<sup>45</sup> In the present work, the  $\text{Fe}^{2+/3+}$  redox couple serves as a stable active material, with facile redox kinetics, for probing cell performance, and under all experimental conditions, the conversion per pass ( $f$ ) is  $f \leq 0.07$ , calculated via 32, where  $I$  is the total current (A) through the cell and  $Q$  is the flow rate ( $\text{m}^3 \text{s}^{-1}$ ).

$$f = \frac{I}{c_{\text{Fe}^{2+}} F Q} \quad [32]$$

The small  $2.55 \text{ cm}^2$  flow cell employed in this work offers key benefits and limitations for quantitating mass transfer in a RFB. Practically, the  $2.55 \text{ cm}^2$  cell requires relatively small quantities of electrolyte materials to perform the desired experiments. Additionally, shrinking the cell permits investigations of flow cell performance in a well-controlled environment, where even flow distribution is anticipated. Under such conditions, mass transfer rates within the porous electrode and flow field channels, as well as between the two domains, can be directly investigated. At scale ( $400\text{--}900 \text{ cm}^2$ ),<sup>46–48</sup> other factors arise that impact mass transfer in a RFB, such as transport losses associated with stack manifolds or uneven reactant distribution across a large electrochemical active area, cannot be probed in the small cell. For example, heterogeneous flow dispersion in filter-press reactor stacks for polysulfide-bromine RFBs have shown non-negligible effects on overall transport rates.<sup>29,30</sup> Finally, non-linear scaling of the pressure drop with increasing geometric active area<sup>46</sup> and shunt currents cannot be studied with small scale cells.<sup>49</sup>

Figure 6 shows representative experimental polarization curves of flow cells in the single electrolyte configuration under various conditions to illustrate several key trends. Note that all experimental polarization measurements have been iR-corrected to remove the resistance contribution due to the membrane, contacts, current collectors, and test leads. In this work, polarization measurements are performed on cells with four flow fields, three iron concentrations, and five flow rates, resulting in sixty unique experimental conditions. Measurements not presented in the main text are available in the Supplementary Material (Figures S5–S8).

Figure 6a demonstrates the effect of flow rate on cell polarization for the FTFF at fixed active species concentration ( $0.2 \text{ M Fe}^{2+/3+}$ ). Increasing flow rate improves electrochemical performance by enhancing the rate of convective mass transfer inside the porous electrode, thus reducing overpotential for a fixed current density. Additionally, increasing flow rate increases the limiting current density for the cell, again due to improved mass transfer in the porous electrode. This behavior is anticipated from prior experimental reports,<sup>17,18,23,28</sup> as well as our model, which indicates that faster mass transfer rates (smaller  $\theta$ ) lead to improved electrochemical performance. Figure 6b illustrates another trend previously reported in literature,<sup>45</sup> where increasing the active material concentration for one field (SFF) at a fixed flow rate ( $2 \text{ mL min}^{-1}$ ) alleviates cell polarization despite a decrease in electrolyte conductivity (Figure 5). Increasing active material concentration increases both the kinetic (Eq. 7) and limiting currents, simultaneously reducing charge and mass transfer losses within the porous electrode. In the particular experimental case outlined in Figure 6b, these kinetic and mass transport gains outweigh the negative impact of decreasing electrolyte conductivity, across the concentration range investigated.

Figure 6c compares cell polarization for the four flow field types at fixed active species ( $0.5 \text{ M Fe}^{2+/3+}$ ) and electrolyte flow rate ( $3 \text{ mL min}^{-1}$ ), revealing more complicated relationships between cell performance and flow field selection. The cell polarization for the PFF is much larger in comparison to the polarization for the three other flow field types, indicating that the PFF offers the worst electrochemical performance. In the PFF design, minimal convective force directly pushes electrolyte into the porous electrode, yielding small

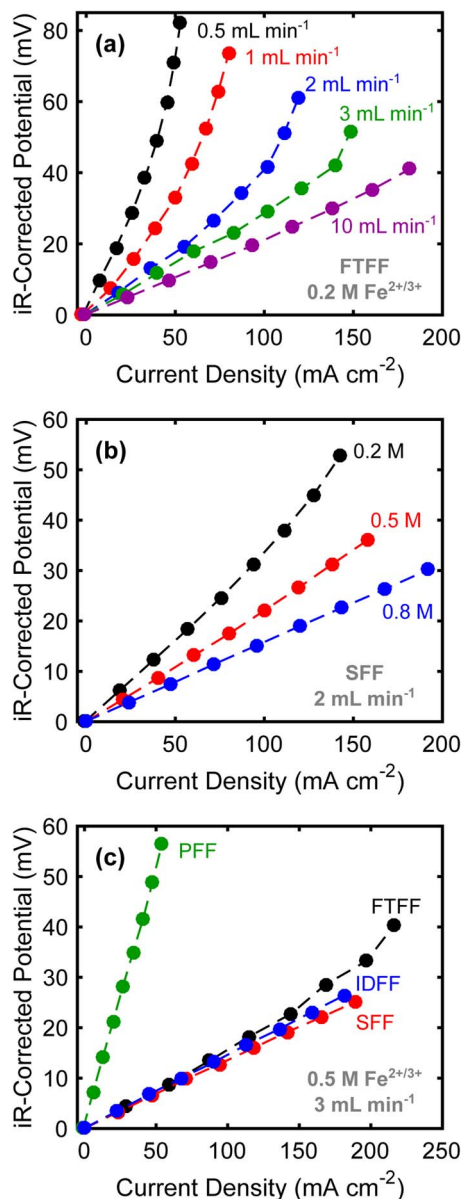


**Figure 6.** Representative iR-corrected polarization curves from the single electrolyte method, experimentally illustrating the effects of flow rate, active species concentration, and flow field design on cell performance. The dashed lines serve only as visual aids. (a) FTFF at various flow rates with fixed active species concentration ( $0.2 \text{ M Fe}^{2+/3+}$ ). (b) SFF at fixed flow rate ( $2 \text{ mL min}^{-1}$ ) with various  $\text{Fe}^{2+/3+}$  concentrations. (c) Various flow fields at fixed flow rate ( $3 \text{ mL min}^{-1}$ ) and fixed active species concentration ( $0.5 \text{ M Fe}^{2+/3+}$ ).

mass transfer rates.<sup>17,18</sup> Under the electrolyte concentration and flow rate conditions implemented in Figure 6c, the FTFF, IDFF, and SFF perform similarly and much better than the PFF. Comparing the flow field performance at fixed electrolyte flow rate, however, is not a good representation because each flow field design displays a different characteristic electrolyte velocity.

To enable a fair comparison among the mass transport characteristics of the various flow fields, we must compare mass transfer coefficients as a function of characteristic electrolyte velocity ( $v_c$ ,  $\text{m s}^{-1}$ ), defined in 33, where  $N_i$  is the number of inlet channels,  $h_c$  is the characteristic flow height, and  $L_c$  is the characteristic flow length (Table I). For the FTFF and IDFF,  $h_c$  is equal to the electrode thickness, whereas for the PFF and SFF,  $h_c$  is the channel height. For the FTFF and IDFF,  $L_c$  is the width and length of the flow field, respectively, whereas for the PFF and SFF,  $L_c$  is the channel width. The calculations



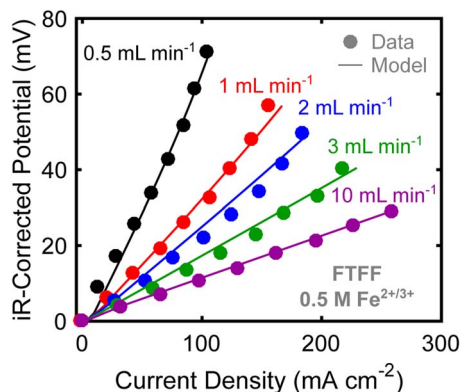
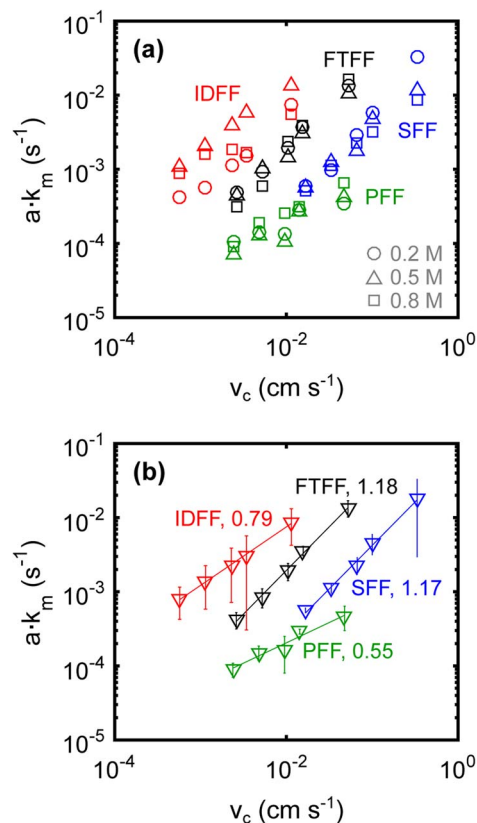
**Table I.** Relevant dimensions for calculating characteristic velocity ( $v_c$ ) through each flow field type.

Flow Field	$N_i$	$h_c$ (mm)	$L_c$ (mm)
FTFF	1	0.228	14
PFF	7	0.5	1
IDFF	4	0.228	16
SFF	1	0.5	1

for characteristic velocity in the FTFF, IDFF, and PFF are identical to a prior publication.<sup>18</sup> Since the FTFF and IDFF designs requires that all electrolyte pass through the electrode, the characteristic velocity for these flow fields describes the mean electrolyte velocity through the porous electrode. By contrast, the characteristic electrolyte velocity for the PFF represents the mean velocity through the flow field channel. The intra-electrode velocity associated with the PFF is anticipated to be near zero,<sup>18</sup> but could be computed numerically using the Brinkman equation. Identifying a characteristic velocity for the SFF, however, is non-trivial given that the SFF design exhibits parallel transport in the channel and porous electrode. As such, we define  $v_c$  for the SFF as the electrolyte velocity in the channel, assuming no electrolyte penetration into the porous electrode, which is similar to the calculation for the PFF. This electrolyte velocity description for the SFF represents the maximum possible pressure drop through the channel.

$$v_c = \frac{Q}{N_i h_c L_c} \quad [33]$$

Using the porous electrode model in conjunction with the experimental polarization data,  $v^2$  and  $\theta$  can serve as fitting parameters to describe the electrode behavior for each experimental condition. For each combination of flow field and iron concentration, a single value of  $v^2$  is fitted alongside five values of  $\theta$  to capture the varying mass transfer rates with changing flow rate. The model is fitted to the experimental data using a sum of squares minimization, more heavily weighing data points at higher flow rates where the experiment best represents the physical assumptions of the model. Specifically, at high flow rates, the single electrolyte flow cell exhibits the lowest conversion per pass, indicating the most uniform concentration profiles and SOC as close to 50% as possible, mimicking the model assumptions. Figure 7 illustrates good fitting of the model to the experimental data for the FTFF with 0.5 M  $\text{Fe}^{2+/3+}$ . As mentioned, each model fit extracts a value of  $v^2$  and  $\theta$  for each individual polarization curve, and these fitting parameters enable a quantitative analysis of mass transfer rates for all experimental conditions examined.

**Figure 7.** Example series of the porous electrode model (solid lines) fitted to the experimental data (●) for a cell with a FTFF and active species concentration of 0.5 M  $\text{Fe}^{2+/3+}$ .**Figure 8.** Computed values of the product of electrode area per unit volume and mass transfer coefficient ( $a \cdot k_m$ ) as a function of the characteristic velocity of the electrolyte in a particular flow field design. (a) All computed values of  $a \cdot k_m$  for each flow field and each active species concentration: 0.2 M  $\text{Fe}^{2+/3+}$  (○), 0.5 M  $\text{Fe}^{2+/3+}$  (△), and 0.8 M  $\text{Fe}^{2+/3+}$  (□). (b) Mean values of  $a \cdot k_m$  (▽) for each flow field and velocity condition with best fit lines (solid lines). The slopes of the best fits are denoted next to the flow field labels.

Extracting mass transfer coefficients from fitted values of  $v^2$  and  $\theta$  begins with substituting the term  $\theta \cdot i_l$  into the definition of  $v^2$ , and subsequently defining  $v^2$  in terms of a mass transfer coefficient and active species concentration in 34. Fitted values of  $v^2$ ,  $\theta$ , and  $a \cdot i_0 \cdot L$  ( $\text{A m}^{-2}$ ) are listed in the Supplementary Material (Tables S1–S6).

$$v^2 = \frac{F a i_0 L^2}{\kappa_{\text{eff}} R T} = \frac{F a (\theta i_l) L^2}{\kappa_{\text{eff}} R T} = \frac{F a (\theta n F k_m c) L^2}{\kappa_{\text{eff}} R T} \quad [34]$$

Since the electrode area per unit volume ( $a$ ) is unknown, we cannot extract independent values of  $k_m$ . The electrode area per unit volume, however, is considered a constant in this work since the same electrode type, pretreatment, and compression ratio are employed across all experiments. The expression  $a \cdot k_m$  ( $\text{s}^{-1}$ ), defined in 35, can provide a relative understanding of mass transfer coefficients for each flow field type and is a common performance factor used to describe flowing electrochemical systems.<sup>23,50</sup>

$$a \cdot k_m = \frac{v^2 \kappa_{\text{eff}} R T}{\theta F^2 L^2 c} \quad [35]$$

Figure 8 shows values of  $a \cdot k_m$  as a function of the characteristic electrolyte velocity through the various flow field designs. In the present model derivation, the mass transfer coefficient is a quantity with no dependence on active material concentration. As a confirmation of the validity of our approach, we plot  $a \cdot k_m$  for each active material concentration individually (Figure 8a), which indicates only small variations in the extracted values of  $a \cdot k_m$  for electrolytes with different active material concentrations, when the flow field and flow rate are fixed. Potential sources of error include slight variations in cell geometry between assemblies, drift in membrane con-

ductivity during the experiment, and the allowable tolerance during curve fitting. Additionally, the flow fields with channels and ribs (e.g., IDFF, PFF, SFF) could lead to inhomogeneous electrode deformation under compression, causing local variations in electrode properties. Furthermore, we note that the model assumptions best describe the FTFF and do not capture the more complex, multidimensional flow patterns in the IDFF, PFF, or SFF, which, in turn, yield poorer model fits than the FTFF case (Figures S5–S8). These differences between the assumed and experimental velocity distributions within the electrode are an additional source of error and likely explain the larger spread in  $a \cdot k_m$  for the non-FTFF cases, however, the reasonably similar quantitative agreement among multiple measurements at different iron concentrations adds confidence to the overall methodology. The level of detail embedded in our polarization model balances sufficient complexity to describe the underlying physics with the flexibility to fit a large number of data sets. Figure 8b plots the mean values of  $a \cdot k_m$  from the three iron concentrations employed for each flow field and flow rate combination, where the error bars represent the standard error from the three concentration measurements. Solid lines in Figure 8b are a best fit line to the experimental data, and numbers next to the legends denote the slopes of the best fit lines. The variation in  $v_c$  for the different flow fields is a result of the treatment in 33 and varying characteristic flow dimensions (Table I); for comparison,  $a \cdot k_m$  is plotted as a function of electrolyte flow rate in the Supplementary Material (Figure S9).

The FTFF offers experimental conditions that best mimic the model assumptions, considering that electrolyte transport through the FTFF is one-dimensional with a uniform velocity profile as a function of position in the electrode. Since the FTFF only invokes transport within a porous electrode (i.e., no flow channels), this flow field also offers the best understanding of transport within the electrode. The FTFF may not be the best choice for implementation in full size RFBs, however, due to an unacceptably large pressure drop through the porous media in cells with large active areas.<sup>18</sup> The FTFF data suggests that the carbon paper employed in this work exhibits  $k_m \propto v_c^{1.18}$  (Figure 8b), which is similar to a study of mass transfer coefficients in a carbon felt electrode, where  $k_m \propto v_c^{0.912}$ .<sup>28</sup> From these relationships,  $k_m$  and  $v_c$  appear to scale in a linear fashion.

Few reports investigate mass transfer in electrochemical reactors with zero-gap<sup>11</sup> flow field designs.<sup>14</sup> The near-linear scaling between mass transfer coefficient and intra-electrode velocity observed in this study and by Xu and Zhao<sup>28</sup> contrast the quantitative investigations of mass transfer coefficients in filter-press (or flow-by) reactors, where an electrolyte gap (typically several millimeters thick) exists between the electrode and membrane.<sup>23,26,29,30</sup> The filter-press design, with flat plate electrodes and inert turbulence promoters, typically affords  $k_m \propto v_c^b$ , where  $0.39 < b < 0.78$ .<sup>23,29,30</sup> Considering transport within only porous media, Fedkiw aggregated data<sup>51</sup> from several studies measuring mass transfer coefficients in packed beds as a function of Peclet number (Pe), defined in 36, where  $d_f$  is the fiber or particle diameter (m) and  $D$  is the diffusion coefficient ( $\text{m}^2 \text{s}^{-1}$ ) of the active species.<sup>52</sup> Fedkiw's analysis highlights that for  $\text{Pe} \leq 20$ , the mass transfer coefficient is linearly proportional to fluid velocity.<sup>53–55</sup> Contrastingly, for  $\text{Pe} \geq 20$ , the mass transfer coefficient is proportional to the cube-root (1/3 power) of velocity,<sup>56–60</sup> which has been observed in some carbon fiber / felt electrodes<sup>61–63</sup> and utilized to estimate mass transfer in prior RFB studies.<sup>18,26,49</sup> Additionally, one study on platinized-titanium mesh electrodes for zinc-cerium RFBs identified this cube-root scaling behavior.<sup>23</sup> While prior data collected for packed beds indicates significant precedent for linear scaling between  $k_m$  and  $v_c$  at low Pe,<sup>53–55</sup> the estimated values for Pe, with the FTFF, in this work are quite high. Assuming a fiber diameter of  $\approx 7 \mu\text{m}$ <sup>25</sup> and typical aqueous diffusion coefficient of  $\approx 5 \times 10^{-6} \text{ cm}^2 \text{ s}^{-1}$ , we estimate  $36 < \text{Pe} < 730$  for the electrolyte velocities applied in the single electrolyte cell. Given the high Pe and linear dependence, we hypothesize that mass transfer within highly porous, fibrous media (e.g., SGL 25AA) resembles that of a packed particle bed with low fluid velocity, and the Pe dependence shifts due to significant morphological differences. These results motivate further study in fibrous porous

media.

$$\text{Pe} = \frac{v_c d_f}{D} \quad [36]$$

The low values of  $a \cdot k_m$  for the PFF reiterate the poor mass transfer rates afforded by that flow field design. The PFF mass transfer coefficients also exhibit the weakest dependence on electrolyte velocity, further supporting the claim that convection does not play a significant role on mass transport in this configuration. By comparison, the FTFF, IDFF, and SFF all achieve mass transfer coefficients that can be  $100\times$  greater than those of the PFF because of forced convection through the porous electrode. In the case of the FTFF, all of the electrolyte is directly pushed through the porous electrode, while the IDFF requires all electrolyte to interface with the porous electrode through a shortened path length.<sup>17,18</sup> The SFF does offer a straight path for the electrolyte to pass through the flow field without entering the electrode, however, the pressure drop across the snaking channel of the flow field is likely so large that electrolyte permeates significantly into the porous electrode.<sup>17</sup>

The IDFF has been regarded in recent literature as the best flow field design to balance electrochemical performance with pressure drop,<sup>17,18,64</sup> although the electrode compression and electrode-to-flow-field contact area must be optimized to mitigate ohmic losses.<sup>18</sup> This flow field relies on dead-ended channels to force electrolyte through a short path of porous electrode, and, as such, comprises multiple flow segments that resemble Poiseuille flow in the channels and Darcy flow in the porous electrode. While all electrolyte must interface with the porous electrode, the highest mass transfer coefficients are not as high as in the FTFF, which is likely due to the non-uniform electrolyte velocity profile within the IDFF; the local electrolyte velocity within the porous electrode is spatially dependent<sup>65</sup> and yields non-uniform mass transfer rates. Additionally, the IDFF exhibits an exponential dependence in between those of the PFF and FTFF designs, hinting that the IDFF behaves as a hybrid of the PFF and FTFF designs. Such hybrid mass transport properties are reasonable given that the pressure drop through the IDFF is also between those of the PFF and FTFF.<sup>18</sup> In fact, the pressure drop through the IDFF can be computed analytically as a product of the pressure drop through a rectangular channel and a geometric factor relating to the porous electrode.<sup>18</sup> For a quantitative comparison of pressure drop through the IDFF, FTFF, and PFF, Darling and Perry offer approximate analytical expressions for each as a function of flow field geometry, electrode permeability, and flow rate.<sup>18</sup> Ultimately, the combination of channels and porous electrode in series makes the IDFF an intriguing mass transfer case that warrants future, detailed study.

Surprisingly, the SFF and FTFF exhibit remarkably similar magnitudes of  $a \cdot k_m$ , and, when plotted as a function of flow rate (Figure S9), the SFF and FTFF data points overlay almost perfectly. The similar mass transfer rates and their nearly identical velocity dependence indicate that the FTFF and SFF are promoting mass transfer in a similar fashion. The pressure drop along the SFF channel is likely so large that nearly all of the electrolyte is forced through the porous electrode, effectively converting the SFF to a FTFF. While pressure drop is not the focus of this work, we calculate that the pressure drop through just the serpentine channel, without any porous media above, evinces a pressure drop that is  $\approx 2.85\times$  higher than the FTFF, indicating that electrolyte flow through the porous electrode is more favorable than through the serpentine channel. Additionally, the single connected channel in the SFF is not a scalable flow field design; the electrolyte penetration into the electrode will depend on the total pressure drop through the single SFF channel, which increases nonlinearly with increasing cell active area. Consequently, when moving toward larger cell designs for practical applications (i.e.,  $> 400 \text{ cm}^2$ ),<sup>46–48</sup> the pressure drop through the SFF will become unacceptable.<sup>17</sup> Exploring SFF designs with multiple, separated snaking segments, such as those commonly used in polymer electrolyte fuel cells,<sup>19</sup> could be a viable option for balancing performance with pressure drop and may offer scalable behavior.

## Conclusions

Mass transfer rates have a significant impact on RFB electrochemical performance, and varying active species concentration, flow rate, flow field design, or electrode morphology will all affect the rate of active species delivery to the electrode surface. Several recent experimental studies have investigated flow field and electrode designs that best improve performance.<sup>17,18,45</sup> Despite experimental interest and the key role of mass transfer in RFBs, mass transfer coefficients in these devices have seldom been reported.<sup>14,28</sup> As such, this study quantifies mass transfer rates in RFBs as a function of active species concentration, flow rate, and flow field design in a systematic fashion. We develop a steady-state, one-dimensional porous electrode model to describe electrode polarization, considering losses due to the electrolyte resistivity, charge transfer, and convective mass transfer. A series of dimensionless plots illustrate how the RFB electrode behaves across a range of exchange and limiting current values, considering variations in overpotential and current distribution throughout the electrode, as well as overall cell polarization (I-V characteristic). The dimensionless nature of the model reduces the physical description of the RFB electrode to two parameters, enabling facile curve fitting of the model to experimental polarization curves. Several key physical assumptions (i.e.,  $\alpha_a = \alpha_c$ ,  $c_{\text{Fe}^{2+}} = c_{\text{Fe}^{3+}}$ ) lead to the concise mathematical form. In conjunction with the model, we implement a single electrolyte diagnostic flow cell technique,<sup>18,37,39,45</sup> with an iron chloride electrolyte, to probe the polarization performance as a function of the aforementioned experimental parameters. Quantitative mass transfer coefficients are extracted by fitting the two model parameters to experimental polarization curves, and the only additional experimental data required is the electrolyte conductivity. In this work, power-law proportionalities between mass transfer coefficient and electrolyte velocity are revealed for four flow field types: flow through, interdigitated, parallel, and serpentine.

Quantifying mass transfer rates for the four common RFB flow fields offers mechanistic insight into transport phenomena, and provides tangible parameters for future engineering optimization. The small 2.55 cm<sup>2</sup> cell permits controlled evaluation of transport phenomena within the porous electrode and flow field, but prohibits study of additional mass transfer effects that only manifest in large-scale cells, such as poor flow distribution. In terms of mechanistic understanding, our FTFF measurements indicate that traditional mass transfer coefficient correlations for packed particle beds are shifted relative to porous carbon paper electrodes. The small  $k_m$  values associated with the PFF and weak flow rate dependence confirms the findings of prior studies that the PFF does not promote forced convection in the porous electrode and is thus unsuitable for implementation in RFBs.<sup>17,18</sup> Additionally, the surprisingly high mass transfer rates associated with the SFF and the intermediate velocity dependence of the IDFF raise interesting questions as to the role of mixed transport in flow field designs. The mass transfer coefficient data and correlations described here can serve as a basis for more advanced computational studies, for optimization of electrolyte flow rate to balance electrochemical performance and pump work, and for more detailed system-level descriptions of technical performance and cost. Moreover, this combined modeling and experimental approach is portable and can be applied to a range of porous electrode materials, electrolyte compositions, and flow field geometries for flow batteries or other flowable systems where reactions occur on the surface of porous media.

## Acknowledgments

This work was supported by the Joint Center for Energy Storage Research (JCESR), an Energy Innovation Hub funded by the United States Department of Energy. J. D. M. acknowledges additional funding from the National Science Foundation Graduate Research Fellowship, and K. M. T. recognizes support from the MIT Summer Research Program. Finally, we appreciate the continued feedback from mem-

bers of the Brushett Group at MIT, as well as from Michael L. Perry of United Technologies Research Center.

## List of Symbols

Symbol	Description	Units
$a$	Electrode area per unit volume	m <sup>2</sup> m <sup>-3</sup>
$b$	Bruggeman coefficient	-
$c$	Concentration	mol m <sup>-3</sup>
$\bar{c}$	Dimensionless concentration	-
$c^s$	Surface concentration	mol m <sup>-3</sup>
$c^\theta$	Standard state concentration	mol m <sup>-3</sup>
$D$	Diffusion coefficient	m <sup>2</sup> s <sup>-1</sup>
$d_f$	Fiber (or particle) diameter	m
$f$	Conversion	-
$F$	Faraday constant	C mol <sup>-1</sup>
$h_c$	Characteristic flow height	m
$I$	Total cell current	A
$i_0$	Exchange current density	A m <sup>-2</sup>
$i_2$	Electrolyte phase current density	A m <sup>-2</sup>
$i_k$	Kinetic current density	A m <sup>-2</sup>
$i_l$	Limiting current density	A m <sup>-2</sup>
$i_n$	Kinetic + mass transfer current density	A m <sup>-2</sup>
$\tilde{j}$	Dimensionless ionic current density	-
$k_a$	Anodic heterogeneous reaction rate	m s <sup>-1</sup>
$k_c$	Cathodic heterogeneous reaction rate	m s <sup>-1</sup>
$k_m$	Mass transfer coefficient	m s <sup>-1</sup>
$L$	Electrode thickness	m
$L_c$	Characteristic flow length	m
$n$	Number of electrons	-
$N_i$	Number of inlet channels	-
Pe	Peclet number	-
$Q$	Flow rate	m <sup>3</sup> s <sup>-1</sup>
$r$	Reaction rate	mol m <sup>-2</sup> s <sup>-1</sup>
$r_k$	Kinetic reaction rate	mol m <sup>-2</sup> s <sup>-1</sup>
$r_{\text{eff}}$	Effective reaction rate	mol m <sup>-2</sup> s <sup>-1</sup>
$R$	Gas constant	J mol <sup>-1</sup> K <sup>-1</sup>
$T$	Temperature	K
$V^\theta$	Standard potential	V
$v_c$	Characteristic electrolyte velocity	m s <sup>-1</sup>
$X$	Position	m
$\tilde{x}$	Dimensionless position	-
<b>Greek</b>		
$\alpha_a$	Anodic transfer coefficient	-
$\alpha_c$	Cathodic transfer coefficient	-
$\beta$	Cathodic transfer coefficient	-
$\delta$	Dimensionless geometric current density	-
$\varepsilon$	Electrode porosity	-
$\eta$	Overpotential	V
$\tilde{\eta}$	Dimensionless overpotential	-
$\kappa$	Electrolyte conductivity	S m <sup>-1</sup>
$\kappa_{\text{eff}}$	Electrode pore phase conductivity	S m <sup>-1</sup>
$v^2$	Dimensionless exchange current density	-
$\varphi$	Overpotential at separator-electrode interface	V
$\Phi_1$	Electrode solid phase potential	V
$\Phi_2$	Electrolyte phase potential	V
$\sigma$	Electrode solid phase conductivity	S m <sup>-1</sup>
$\theta$	Ratio of exchange to limiting current densities	-

## References

1. B. Dunn, H. Kamath, and J.-M. Tarascon, *Science*, **334**, 928 (2011).
2. I. Gyuk et al., *Grid Energy Storage*, US Department of Energy, Washington DC, (2013) [http://energy.gov/sites/prod/files/2013/12/15/20131215\\_Grid%20Energy%20Storage%20December%202013.pdf](http://energy.gov/sites/prod/files/2013/12/15/20131215_Grid%20Energy%20Storage%20December%202013.pdf).
3. P. Denholm, E. Ela, B. Kirby, and M. Milligan, *The Role of Energy Storage with Renewable Electricity Generation*, NREL/TP-6A2-47187, (2010).

4. A. Z. Weber et al., *J. Appl. Electrochem.*, **41**, 1137 (2011).
5. P. Leung et al., *RSC Adv.*, **2**, 10125 (2012).
6. A. Parasuraman, T. M. Lim, C. Menictas, and M. Skyllas-Kazacos, *Electrochimica Acta*, **101**, 27 (2013).
7. W. Wang et al., *Adv. Funct. Mater.*, **23**, 970 (2013).
8. R. M. Darling, K. G. Gallagher, J. A. Kowalski, S. Ha, and F. R. Brushett, *Energy Environ. Sci.*, **7**, 3459 (2014).
9. R. Dmello, J. D. Milshtein, F. R. Brushett, and K. C. Smith, *J. Power Sources*, **330**, 261 (2016).
10. V. Viswanathan et al., *J. Power Sources*, **247**, 1040 (2014).
11. D. S. Aaron et al., *J. Power Sources*, **206**, 450 (2012).
12. Q. H. Liu et al., *J. Electrochem. Soc.*, **159**, A1246 (2012).
13. K. J. Kim et al., *J. Mater. Chem. A*, **3**, 16913 (2015).
14. X. L. Zhou, T. S. Zhao, L. An, Y. K. Zeng, and L. Wei, *J. Power Sources*, **339**, 1 (2017).
15. J. Houser, J. Clement, A. Pezeshki, and M. M. Mench, *J. Power Sources*, **302**, 369 (2016).
16. J. D. Milshtein et al., *Energy Env. Sci.*, **9**, 3531 (2016).
17. C. R. Dennison, E. Agar, B. Akuzum, and E. C. Kumbur, *J. Electrochem. Soc.*, **163**, A5163 (2016).
18. R. M. Darling and M. L. Perry, *J. Electrochem. Soc.*, **161**, A1381 (2014).
19. X. Li and I. Sabir, *Int. J. Hydrog. Energy*, **30**, 359 (2005).
20. M. L. Perry, R. M. Darling, and R. Zaffou, *ECS Trans.*, **53**, 7 (2013).
21. Online: "ARPA-E | Breakthrough flow battery stack," arpa-e.energy.gov/?q=slick-sheet-project/breakthrough-flow-battery-cell-stack; cited: March 29, 2017.
22. J. Houser, A. Pezeshki, J. T. Clement, D. Aaron, and M. M. Mench, *J. Power Sources*, **351**, 96 (2017).
23. L. F. Arenas, C. P. de León, and F. C. Walsh, *Electrochimica Acta*, **221**, 154 (2016).
24. J. González-García et al., *Ind. Eng. Chem. Res.*, **37**, 4501 (1998).
25. I. V. Zenyuk, D. Y. Parkinson, L. G. Connolly, and A. Z. Weber, *J. Power Sources*, **328**, 364 (2016).
26. H. Zhou, H. Zhang, P. Zhao, and B. Yi, *Electrochimica Acta*, **51**, 6304 (2006).
27. X. Li, *Electrochimica Acta*, **170**, 98 (2015).
28. Q. Xu and T. S. Zhao, *Phys. Chem. Chem. Phys.*, **15**, 10841 (2013).
29. C. Ponce-de-León, G. W. Reade, I. Whyte, S. E. Male, and F. C. Walsh, *Electrochimica Acta*, **52**, 5815 (2007).
30. C. Ponce-de-León, I. Whyte, G. W. Reade, S. E. Male, and F. C. Walsh, *Aust. J. Chem.*, **61**, 797 (2008).
31. Q. Zheng et al., *Appl. Energy*, **132**, 254 (2014).
32. K. W. Knehr, E. Agar, C. R. Dennison, A. R. Kalidindi, and E. C. Kumbur, *J. Electrochem. Soc.*, **159**, A1446 (2012).
33. Q. Zheng, F. Xing, X. Li, G. Ning, and H. Zhang, *J. Power Sources*, **324**, 402 (2016).
34. J. S. Newman and C. W. Tobias, *J. Electrochem. Soc.*, **109**, 1183 (1962).
35. J. A. Trainham and J. Newman, *J. Electrochem. Soc.*, **124**, 1528 (1977).
36. W. Tiedemann and J. Newman, *J. Electrochem. Soc.*, **122**, 1482 (1975).
37. C.-N. Sun et al., *J. Electrochem. Soc.*, **161**, A981 (2014).
38. J. D. Milshtein, J. L. Barton, R. M. Darling, and F. R. Brushett, *J. Power Sources*, **327**, 151 (2016).
39. R. M. Darling and M. L. Perry, *ECS Trans.*, **53**, 31 (2013).
40. J. Newman and W. Tiedemann, *AIChE J.*, **21**, 25 (1975).
41. J. Newman and K. E. Thomas-Alyea, *Electrochemical Systems*, 3rd ed., p. 210, John Wiley & Sons, Inc., Hoboken, (2004).
42. W. M. Haynes, *CRC handbook of chemistry and physics: A ready-reference book of chemical and physical data*, 97th ed., CRC Press, Inc., Boca Raton, (2017).
43. Z. Galus and R. N. Adams, *J. Phys. Chem.*, **67**, 866 (1963).
44. J. D. Milshtein, S. M. Fisher, T. M. Breault, L. T. Thompson, and F. R. Brushett, *ChemSusChem*, **10**, 2080 (2017).
45. A. M. Pezeshki, R. L. Sacci, F. M. Delnick, D. S. Aaron, and M. M. Mench, *Electrochimica Acta*, **229**, 261 (2017).
46. E. Knudsen, P. Albertus, K. T. Cho, A. Z. Weber, and A. Kojic, *J. Power Sources*, **299**, 617 (2015).
47. X. Wu et al., *J. Solid State Electrochem.*, **21**, 429 (2017).
48. P. Zhao et al., *J. Power Sources*, **162**, 1416 (2006).
49. R. M. Darling, H.-S. Shiau, A. Z. Weber, and M. L. Perry, *J. Electrochem. Soc.*, **164**, E3081 (2017).
50. D. Pletcher and F. C. Walsh, *Industrial Electrochemistry*, 2nd ed., p. 81, Springer Science+Business Media, LLC, (1993).
51. P. S. Fedkiw, "Mass transfer controlled reactions in packed beds at low Reynolds numbers," thesis, University of California, Berkeley (1978).
52. R. B. Bird, W. E. Stewart, and E. N. Lightfoot, *Transport Phenomena*, 2nd ed., p. 316, John Wiley & Sons, Inc., New York, (2007).
53. M. Bar-Ilan and W. Resnick, *Ind. Eng. Chem.*, **49**, 313 (1957).
54. T. H. Hsiung and G. Thodos, *Int. J. Heat Mass Transf.*, **20**, 331 (1977).
55. K. Kato, H. Kubota, and C. Y. Wen, *Chem. Eng. Program Symp. Ser.*, **66**, 87 (1970).
56. C. Appel and N. Bonanos, *J. Eur. Ceram. Soc.*, **19**, 847 (1999).
57. S. Kumar, S. N. Upadhyay, and V. K. Mathur, *Ind. Eng. Chem. Process Des. Dev.*, **16**, 1 (1977).
58. J. E. Williamson, K. E. Bazaire, and C. J. Geankoplis, *Ind. Eng. Chem. Fundam.*, **2**, 126 (1963).
59. E. J. Wilson and C. J. Geankoplis, *Ind. Eng. Chem. Fundam.*, **5**, 9 (1966).
60. S. N. Upadhyay and G. Tripathi, *J. Chem. Eng. Data*, **20**, 20 (1975).
61. D. Schmal, J. Van Erkel, and P. J. Van Duin, *J. Appl. Electrochem.*, **16**, 422 (1986).
62. K. Kinoshita and S. C. Leach, *J. Electrochem. Soc.*, **129**, 1993 (1982).
63. B. Delanghe, S. Tellier, and Astruc, *Electrochimica Acta*, **35**, 1369 (1990).
64. M. L. Perry, "Flow battery with interdigitated flow field," US Pat. US 91666243 B2, Filed December 18, 2009.
65. A. Kazim, H. T. Liu, and P. Forges, *J. Appl. Electrochem.*, **29**, 1409 (1999).